X-ray nano-computed tomography of electrochemical conversion in lithium-ion battery

Daniele Di Lecce[a], Stanislav Levchenko[b], Francesco Iacoviello[a], Dan J.L. Brett[a], Paul R. Shearing[a,*], and Jusef Hassoun[b,c,*]

[a] *Electrochemical Innovation Lab, Department of Chemical Engineering, University College London, Torrington Place, London WC1E 7JE, United Kingdom*

[b] *Department of Chemical and Pharmaceutical Sciences, University of Ferrara, Via Fossato di Mortara, 17, 44121, Ferrara, Italy.*

[c] *National Interuniversity Consortium of Materials Science and Technology (INSTM), University of Ferrara Research Unit, University of Ferrara, Via Fossato di Mortara, 17, 44121, Ferrara, Italy.*

*Corresponding authors: jusef.hassoun@unife.it; p.shearing@ucl.ac.uk.

Abstract

In this work we investigate a nanometric copper oxide (CuO) anode for lithium-ion batteries by combining electrochemical measurements and *ex situ* X-ray computed tomography (CT) at the nanoscale. The electrode reacts by conversion at about 1.2 and 2.4 V *vs.* Li^+/Li during discharge and charge, respectively, delivering a capacity between 500 mAh g^{-1} to over 600 mAh g^{-1}. Three-dimensional nano-CT imaging reveals substantial reorganization of the CuO particles and precipitation of a Li^+-conducting film suitable for a possible application in the battery. Therefore, a lithium-ion cell exploiting the high capacity of the conversion process is assembled by using a high-performance $LiNi_{0.33}Co_{0.33}Mn_{0.33}O_2$ cathode reacting at 3.9 V *vs.* Li^+/Li. The cell is proposed as energy-storage system with average working voltage of about 2.5 V, specific capacity of 170 mAh $g_{cathode}^{-1}$, efficiency exceeding 99%, and very stable cycling.

Table of Contents

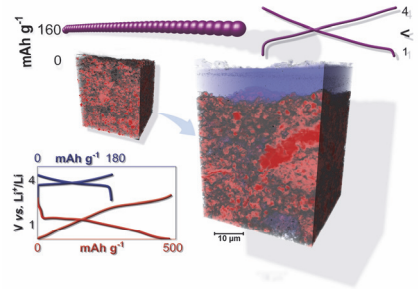

An advanced 3D imaging: X-ray computed tomography at the nanoscale sheds light on the electrochemistry of CuO, involving nanoparticles reorganization and precipitation of a passivation layer. A CuO/$LiNi_{0.33}Co_{0.33}Mn_{0.33}O_2$ cell delivering almost 170 mAh $g_{cathode}^{-1}$ at 2.5 V suggests a possible application of nanometric metal oxides as anodes for lithium-ion batteries.

Keywords

X-ray computed tomography; Nanoparticle; Copper Oxide; $LiNi_{0.33}Co_{0.33}Mn_{0.33}O_2$; Electrochemistry

Introduction

The lithium-ion battery (LIB) is amongst the most relevant and attractive electrochemical energy-storage systems, which is widely adopted in devices ranging from power drills to electronics, medical devices, and electric vehicles.[1,2] Further need for efficient rechargeable batteries has been triggered by the rapid adoption of intermittent renewable energy technologies.[3] In this view, the research for alternative lithium-ion battery configurations beside the most common one, which is based on graphite anode and lithium cobalt oxide cathode,[4] is considered of crucial importance to mitigate the increasing economic and environmental challenges.[5] Among the several alternative cathodes proposed by literature,[6] lithium enriched layered oxides based on various metals,[7] high-voltage spinel-structure metal oxides,[8] and phospho-olivine polyanionic electrodes[9] have been considered the most suitable materials. In particular, metal-substituted layered oxides, in which cobalt is partly replaced by manganese and nickel according to various ratios, have been indicated as attractive

cathodes due to their lower cost, mitigated environmental impact and higher electrochemical stability at large intercalation degree compared to conventional $LiCoO_2$.[10] Several anode materials with improved lithium-storage characteristics have been proposed to replace graphite in order to increase the LIBs energy density.[11] Among the negative electrodes, Li-alloy materials such as silicon, tin, and antimony, have demonstrated the most relevant properties in terms of working voltage and specific capacity.[12] Relevantly, the large volume changes occurring during the electrochemical Li-alloying process were successfully buffered by sophisticated nanostructures benefitting from top-down and bottom-up material-engineering approaches to promote the electrode stability.[13]

Metal oxides, such as CuO,[14] NiO[15] and Fe_2O_3,[16] may reversibly exchange more than 1 equivalent of lithium according to a multi-electron conversion mechanism, also called displacement, evolving within a wide potential region with remarkable specific capacity.[17] Therefore, the above mentioned oxides have been proposed as alternative to graphite and Li-alloys for application as anodes in lithium-ion batteries characterized by high capacity and, at the same time, low cost.[18] However, the relevant voltage hysteresis between charge and discharge processes[19] and the modest stability of the conversion reaction due to significant structural[20] and volume changes,[21] has so far hindered the application of these intriguing electrodes in efficient full Li-ion cells.[22]

Recently, synthetic approaches for nanostructured metal oxides capable of retaining structural integrity and ensuring electrode stability have been developed, which has only partly mitigated the voltage hysteresis issue.[16,23–26] Indeed, the complex displacement reaction pathway involving massive electrode reorganizations actually affects the electrochemical potential stability upon prolonged cycling and leads to capacity decay,[24,27] thus limiting the practical applications of metal oxide anodes.[28,29]

Advanced *ex* and *in situ* measurements have promoted the fundamental understanding of the structural and morphological modifications, as well as of the metal oxide composition effects on the conversion reaction features.[21,27,30–33] Among the various investigation approaches, three-dimensional imaging at the micro- and nanoscale may actually shed light on the particle evolution

throughout the lithium-exchange process and reveal crucial morphological parameters for electrode modelling, such as the phase volume fraction and the particle size distribution.[34–36] In particular, X-ray nano-computed tomography (CT) allows a detailed reconstruction of the spatial distribution of the various electrode components,[37] and provides useful qualitative compositional information associated with the attenuation of the incident beam.[38] Insights of the displacement process may pave the way for a performance enhancement aiming at the effective employment of metal oxides as anodes in efficient and stable full-cells, which is considered essential to demonstrate the applicability of this class of materials.[11] Therefore, we have studied in this work structure, morphology and electrochemical response of a nanometric copper oxide (CuO) electrode. The material reorganizations due to conversion with lithium upon charge/discharge cycles have been thoroughly characterized through *ex situ* nano-CT and the high reversibility of the electrochemical reaction is further assessed in full-cell configuration with a $LiNi_{0.33}Co_{0.33}Mn_{0.33}O_2$ cathode. Although the latter study may not be directly related to the fundamental characterization of the electrochemical conversion of CuO, full-cell demonstration may advantageously link basic and applied research on lithium-ion battery materials. Thus, the deeper insight on the structural evolution of the electrode in the cell provided by X-ray CT and electrochemistry can actually allow an advanced lithium-ion battery.

Results and discussion

Prior to electrochemical characterization, the nanometric CuO has been studied in terms of structure and morphology (Fig. 1) in order to preliminarily evaluate the suitability of the material for cell application. The X-ray diffraction (XRD) patterns of Fig. 1a show pronounced crystallinity, and a primary CuO unit cell with monoclinic lattice which appertains to the C1c1 (9) space group according to the ICDD (PDF #80-1916). Furthermore, scanning electron microscopy (SEM) images (Fig. 1b, c) reveal primary sub-micrometric agglomerates with a size approaching 500 nm of nanometric particles (70 nm), which are clearly evidenced by the transmission electron microscopy (TEM) images of Fig. 1c,e. The selected area diffraction pattern (SADP) of the nanoparticles shows a crystalline structure

in agreement with XRD (see Fig. 1e inset). This agglomerated nanometric morphology and the defined crystalline structure are expected to ensure suitable behavior of the CuO electrode in a lithium cell.[24] Indeed, the nanometric particle size may mitigate the volume changes of the electrode during cycling[39] and enhance the rate capability,[40] while the presence of agglomerates prevents possible electrode pulverization[41] and limits the reactivity of the material at the electrode/electrolyte interphase that is generally promoted by the presence of dispersed nanoparticles, in particular at the electrode surface.[13] Relevantly, the absence of impurities or carbonaceous matrixes in the electrode formulation (see experimental section) may actually limit possible parasitic reactions, which generally lead to a remarkable decrease of the coulombic efficiency of the material in lithium cells, thus hindering its possible use in stable full Li-ion cells.[42,43]

Figure 1

Figure 2 shows the cyclic voltammetry (CV) response (a) and the Nyquist plots of electrochemical impedance spectroscopy (EIS) measurements (b) performed at the OCV, after the first, second and third cycle in three-electrode lithium cell using the nanometric CuO as the working electrode. The voltammograms of Fig. 2a reveal a first cathodic scan characterized by the presence of a strong reduction peak at about 1.1 V *vs.* Li^+/Li and a shoulder at about 0.8 V *vs.* Li^+/Li, which are mainly ascribed to the conversion of CuO to metallic Cu and Li_2O, as widely described in literature.[44–48] CV reveals additional irreversible processes occurring throughout the first discharge at about 1.6, 1.1, and 0.8 V *vs.* Li^+/Li, which may be attributed to electrolyte reduction with consequent formation of a SEI layer at the electrode surface,[49] as well as to possible rearrangements within the electrode. A further peak at potential values close to 0 V *vs.* Li^+/Li suggests insertion in the Super P conductive additive[46] along with possible electrolyte decomposition[50] at the lowest potential values. During the first anodic scan, the voltammogram shows a minor oxidation peak at about 0.8 V *vs.* Li^+/Li, and a main peak at about 2.5 *vs.* Li^+/Li due to the electrochemical charge of the electrode material.[44–48] The subsequent voltammetry cycles reveal a reduction peak around 1.3 V *vs.* Li^+/Li during the cathodic scan, which is reversed into a broad oxidation peak around 2.5 V *vs.*

Li^+/Li during the anodic scan. These two peaks, in addition to minor reversible peaks at about 0.8 V *vs.* Li^+/Li during reduction and 2.0 V *vs.* Li^+/Li during oxidation, are attributed to the multi-electron conversion reaction between CuO and Li (equation (1)), according to a mechanism already studied in literature.[44,48]

$$CuO + 2Li \rightarrow Cu + Li_2O \quad (1)$$

It is worth mentioning that the reaction pathway includes intermediate steps involving minor lithiation of CuO at the higher voltages, *i.e.*, above 2 V, to form a copper oxide described herein as Li_yCuO ($y < 0.1$) in which Cu^{II} is partially reduced to Cu^I,[44] followed by a massive electrode reorganization ascribed to conversion with the formation of a $Cu^I{}_2O$ phase and eventually metallic Cu embedded into a Li_2O matrix.[21] These processes lead to a significant volumetric change upon discharge, which may adversely affect the reversibility of the conversion reaction upon prolonged cycling.[21] Furthermore, literature studies have suggested a partially reversible conversion of CuO, due to the presence of Cu^I in the fully charged electrode.[31] Fig. 2a reveals a remarkable voltage hysteresis, as typically attributed to the reaction pathways between oxidation and reduction which involves relevant structural change.[51] In order to further investigate the electrode evolution upon cycling we have performed EIS measurements throughout the CV. The related Nyquist plots in Fig. 2b evidence at the OCV the typical profile expected for a blocking electrode, characterized by the presence of a semicircle at the medium-high frequencies (inset of Fig. 2b) due to the electrode/electrolyte interphase, with a resistance of 21 Ω, and an almost vertical line ascribed to the geometric cell capacitance.[47] After the first voltammetry cycle, the interphase resistance increases up to 95 Ω due to the SEI growth and the contribution of the charge transfer.[52] A possible overlapping of the related semicircles does not allow us to clearly discern the responses of SEI and charge transfer, which are expected at high and medium frequencies, respectively. Furthermore, a tilted line ascribed to Warburg-type lithium ions diffusion phenomena may be observed in the low frequency region.[47] The Nyquist plots after the second and third cycles in Fig. 2b reveal the same profile of the one

observed after the first complete voltammetry scan, however with an interphase resistance increasing up to 151 and 211 Ω, respectively. The increase of the cell resistance may be likely associated both with the growth of a SEI layer at the electrode surface and with the above mentioned modification of the nanometric CuO electrode during conversion reaction which unavoidably lead to the relevant charge/discharge polarization observed by voltammetry in Fig. 2a.[47,52] Despite the relatively large potential hysteresis and the resistance increase by cycling, the CV trends and the interphase characteristics observed in Fig. 2 appear suitable for battery application,[47,52] which is hereafter proven by galvanostatic cycling of the nanometric CuO electrode in lithium cell.

Figure 2

Figure 3 reports the cycling performance of CuO in lithium half-cells at various currents. A rate capability test is preliminarily performed by changing the current from C/10 to 1C, and reported in terms of voltage profile (Fig. 3a) and corresponding cycling response with coulombic efficiency (Fig. 3b). During the first cycle (inset of Fig. 3a), the voltage profile shows a discharge plateau at about 1.1 V extending up to about 800 mAh g^{-1}, which is followed by a progressive slope down to 0.02 V leading to a specific capacity slightly exceeding 1000 mAh g^{-1}. This shape, corresponding to the processes already observed by CV in Fig. 2, is reversed during charge into a tilted line, extending from 0.01 V to 2 V, with a capacity of about 200 mAh g^{-1}, and a plateau above 2 V at the end of which the capacity reaches a value approaching 400 mAh g^{-1}. Hence, the first cycle is characterized by a low coulombic efficiency (Fig. 3b) which is ascribed both to the irreversible formation of the SEI and to the nature of the conversion process involving changes of the electrode structure, likely leading to a partial loss or insulation of the active material.[22,53] The second cycle (not reported) as well as the steady-state cycles at C/10 (Fig. 3a) are characterized by a different, more sloped profile during discharge with respect to the first one, while similar charge profiles are observed with a remarkably stable capacity of about 540 mAh g^{-1} (80 % of the theoretical capacity) and a coulombic efficiency approaching 100% (Fig. 3b). It is worth mentioning that both the change of the discharge profiles and the increase of the reversible capacity from 400 mAh g^{-1} to 540 mAh g^{-1} at the steady

state indicate progressive electrode modifications during cycling,[22] which are accompanied by a gradual electrochemical activation of part of the CuO inactive during the initial stages of the cycling test.[54] The tests at C-rate higher than C/10 lead to the expected slight increase of polarization (Fig. 3a) and a decrease of delivered capacity (Fig. 3b) to 480, 438, 380 and 341 mAh g^{-1} at C/5, C/3, C/2 and 1C rate, respectively, while the efficiency permanently approaches 100% upon 1 cycle after each current change. Remarkably, the reversible capacity delivered at low C-rate (540 mAh g^{-1} at C/10) exceeds the one of the commercial graphite conventionally used in lithium-ion cell (372 mAh g^{-1}),[5] while the value at the highest C-rate (341 mAh g^{-1} at 1C) approaches the graphite capacity at a significantly higher specific current (1C = 674 mA g^{-1} for CuO and 372 mA g^{-1} for graphite).[5] Furthermore, the cell fully recovers its reversible capacity by lowering back the current to the initial value of C/10 (Fig. 3b), thus accounting for an enhanced stability of the electrode material during cycling.

Galvanostatic tests at fixed current values are performed in order to evaluate the cycle life of the material in lithium cell (Fig. 3c-h). The voltage profiles (Fig. 3c) and the cycling trend with coulombic efficiency (Fig. 3d) of the measurements performed at C/20 reveal the above mentioned irreversible capacity during the first cycle in addition to an activation process,[54] prolonged for about 30 cycles, which leads to a steady-state capacity of about 620 mAh g^{-1} (92% of the theoretical value) and a coulombic efficiency approaching 100% (Fig. 3d). After the first charge/discharge cycle, the cell shows an average working voltage of about 1.8 V and a stable profile reflecting the above mentioned capacity increase (Fig. 3c). The cells cycled at C/10 (Fig. 3e,f) and C/5 (Fig. 3h,g) evidence a very similar trend of both voltage profile and cycling response, despite a lower reversible capacity due to increasing polarization by raising currents, that is, 570 and 480 mAh g^{-1}, respectively. It is worth mentioning that the activation trend and duration appear to be affected by the current value which likely influences the kinetics of the electrode material reorganization.[55]

Figure 3

In summary, the results of Figs. 2 and 3 reveal reversible conversion processes with high coulombic efficiency, considered suitable for possible application,[5] and suggest a gradual electrode rearrangement promoted by the well-known structural changes associated with the displacement reaction[22] leading to activation by cycling. Such a reorganization of Me_xO_y compounds upon reaction with lithium via conversion in cell has been already investigated by literature works combining structural, morphological, and electrochemical techniques, which evidenced the formation of metallic nanodomains within a Li_2O matrix during discharge along with significant volume change and deposition of a SEI layer at low potential *vs*. Li^+/Li.[22] Accordingly, the particle size of the active material modifies during subsequent charge/discharge cycles.[31] Herein, the three-dimensional electrode structure has been imaged by means of X-ray nano-CT in order to further shed light on the CuO particle evolution upon cycling. A micro-CT scan of a pristine sample reveals the main features of the electrode, consisting of highly attenuating (bright) micrometric particles surrounded by a finely dispersed mixture of CuO, PVDF, and carbon, as well as lowly attenuating (dark) cracks and micropores (see the related cross-sectional slice in Fig. S1 of the Supporting Information). Whilst the large field of view (about 470 μm) provides a reasonable representation of the bulk electrode morphology, the relatively low resolution of X-ray micro-CT (voxel size about 507×507×507 nm^3) does not allow us to discern the CuO nanostructures, formed by sub-micrometric agglomerates of particles with size of about 70 nm according SEM and TEM (see Fig. 1b-e). On the other hand, X-ray nano-CT advantageously reveals more detailed characteristics of the CuO aggregates within a field of view of about 65 μm due to a voxel axis as low as 63 nm.

Microscale pillars have been prepared by laser milling a pristine sample as well as electrodes after 1 and 10 galvanostatic cycles at a C/5 rate (1C = 674 mA g^{-1}) in a lithium-half cell (see the experimental section and Fig. S2 in the Supporting Information for further details). SEM-EDS analysis of the laser-milled electrodes confirms the morphological features observed in Fig. 1b-c and suggests a significant change of the electrode morphology upon 10 cycles, that is, a slight growth and agglomeration of the CuO particles after 1 cycle, followed by formation of a thick SEI layer over the

electrode surface after 10 cycles (see Fig. S2 in the Supporting Information). The electron backscattering provides qualitative information about the sample composition, suggesting a passivation layer mainly located over the electrode and formed by light elements (see Fig. S2o-p related to the electrode after 10 cycles). Meanwhile, the corresponding EDS (Fig. S2q) clearly indicates the presence of Cu, C, O, and F in the electrodes, and reveals a different elemental distribution after 10 cycles for SEI layer and electrode bulk in agreement with the SEM images. Indeed, SEI shows high C content and bulk evidences high Cu content, while O and F are observed in both sides, according to the electrode formulation and the already reported composition of the SEI in conventional alkyl-carbonate solutions using $LiPF_6$.[56]

Panels a, b and c of Fig. 4 show cross-sectional slices orthogonal to the current collector obtained from nano-CT imaging on pristine CuO, CuO after 1 cycle and CuO after 10 cycles, respectively. The related grayscale histograms of Fig. 4d suggest a gradual change of the X-ray attenuation in the samples as a result of cycling, namely a decrease of attenuation for the high-contrast domains. Since the nano-CT scans have been carried out under the same accelerating voltage and exposure time, the difference in terms of grayscale value for the various domains may be directly related to the attenuation coefficients, thus providing information about changes of density of the observed materials throughout cycling.[38] Based on the results of the structural, morphological and electrochemical characterization above reported, four phases corresponding to the peaks in Fig. 4d at increasing grayscale values (increasing attenuation) have been identified by using a thresholding method,[38] and attributed to pores/exterior, SEI, carbon-binder domain, and copper oxide. The similar X-ray scattering coefficient of pores/exterior, SEI, and carbon-binder domain might lead to some degree of uncertainty in the segmentation. Herein we have identified the grayscale cutoffs between the lowly attenuating domains as the minima of the histograms in Fig. 4d.[38] Furthermore, the grayscale curves may allow us to distinguish two CuO domains. Thus, the peak at middle-high grayscale values and shoulder at high grayscale values are respectively attributed to a low-density CuO domain, represented by partially agglomerated, small, grey particles in panels a-c, and to a high-

density CuO domain, consisting of large, bright particles in panels a-c. The observation of highly-attenuating, large particles beside the nanoparticles agglomerates (observed in Fig. 1b-e) is in agreement with the micro-CT results. Further scans of pristine electrodes prepared without laser milling are consistent with Fig. 4a, thereby excluding possible effects of the high-energy micromachining on the sample composition (see the experimental section and Fig. S3 in the Supporting Information for additional details). It is worth mentioning that the CuO domains in the electrodes after 1 and 10 cycles reasonably include Cu^{I}-containing phases due to the partial irreversibility of conversion process according to Figs. 2 and 3.[31] As expected, the ratio between the grayscale peak values of carbon-binder to pores is approximately constant for the three samples, while that of CuO to pores gradually decreases after cycling, thereby suggesting a decrease of copper oxide density.[38] However, the voxel resolution does not allow observation of possible nanoporosity, which might partially account for the observed X-ray attenuation values within the CuO domains. Based on these considerations and on literature works,[21,31,44,48] low-density copper oxide might include nanopores as well as unreacted Cu_2O and Li_2O species. Therefore, the two CuO domains shown by both nano- and micro-CT might be actually formed by various phases whose nanostructure cannot be effectively detected within our experimental conditions. Accordingly, the observation of low and high density CuO and their relative changes upon cycling should be considered as a significant qualitative information about the nanostructure reorganization undergone by the active material, leading to a decrease of the X-ray attenuation, rather than a rigorous identification of two distinct phases. Thus, a clear separation of the two domains is not straightforward. Herein we have arbitrarily designed the greyscale cutoffs based on the shape of the histogram curve (Fig. 4d).

Figure 4

The segmented cross-sectional slices corresponding to panels a, b and c of Fig. 4, shown in panels e, f and g, respectively, display a rearrangement of the CuO aggregates after cycling, along with formation of an SEI layer over the surface and within the porosity of the electrode. In agreement with the EIS results revealing a constant increase of the electrode/electrolyte interphase resistance by

cycling (Fig. 2), the passivation layer gradually grows after the 1st cycle, eventually leading to a low-density film likely including nanopores.[57] On the other hand, the low thickness of the SEI after the 1st discharge/charge does not allow a clear observation by nano-CT. Despite the fact that the thickness remarkably increases after the 10th cycle, the SEI exhibits fast Li^+-transport properties leading to suitable charge transfer as demonstrated by galvanostatic tests in Figs. 3 and S2a (Supporting Information). The phase volume fraction of a cropped cube excluding the electrode surface has been calculated and reported in Fig. 4h. The analysis reveals a clear trend upon cycling, characterized by a gradual increase of the volume fraction of copper oxide associated with a contraction of the carbon-binder domain, while the pores are progressively filled by the electrolyte decomposition products forming the SEI.[57]

Volume rendering of the datasets (Fig. 5a-c) evidences the electrode evolution in the cell, and suggests substantial modifications upon 10 cycles due to SEI growth and copper oxide agglomeration. These observations are confirmed by the continuous particle size distribution analysis of cropped sub-volumes reported in Fig. 5d,e (see the experimental section for further information), which reveals a growth of copper oxide aggregates with estimated radii ranging from 300 to 700 nm as well as a decrease of the number of particles smaller than 300 nm. Such changes are observed for both copper oxide domains, alongside with a decrease of the number of high-density CuO particles larger than 800 nm.

Figure 5

Gradual nanograin aggregation in CuO-based anodes has been already suggested by studies conducted by coupling *in situ* TEM and electrochemical measurement,[31] which evidenced severe rearrangements upon the first lithiation/delithiation process, leading to formation of Cu_2O after charge and eventual increase of the particle size after a few cycles. These electrode modifications typically involve huge volume variations[21] and may actually influence the cycling behavior in terms of reversible capacity.[12] It is worth mentioning in this respect that partial oxidation of Cu^0 to Cu^I during charge may decrease the lithium exchange ability through displacement reaction of CuO materials

due to the relatively low reversible capacity of Cu_2O (that is, 375 mAh g^{-1}). Instead, our results indicate a beneficial effect of the massive reorganizations on the cycling ability of CuO nano-powders, with gradual activation and stabilization of the capacity above 500 mAh g^{-1} by cycling (see Fig. 3).

Despite the remarkable hysteresis associated with the complex conversion mechanism which may hinder the application in practical full-cells, a proper selection of cathode material, experimental setup adopted for cell assembling and testing, as well as a careful tuning of the electrodes weight to avoid cell instability, is expected to mitigate the intrinsic issues of metal oxide anodes.[5] Accordingly, a lithium-ion cell has been herein assembled by coupling the nanometric CuO anode and a $LiNi_{0.33}Co_{0.33}Mn_{0.33}O_2$ cathode as shown in Figure 6. The cathode belongs to a widely-investigated new generation of layered compounds including various metals with improved characteristics compared to $LiCoO_2$, such as high specific capacity extended up 170 mAh g^{-1}, high rate capability, stable cycling trend, and a suitable voltage profile centered at about 3.9 V *vs*. Li^+/Li (see Fig. 6a).[42] Fig. 6b shows the actual balance used for full-cell assembly, and the steady-state voltage profile of anode (blue line) and cathode (red line). The graphs evidence a cathode areal capacity matching at the steady state a value of about 62% of the anode one, according to the adopted mass balance, that is, 4.0 mg cm^{-2} and 2.5 mg cm^{-2}, respectively, as normalized to the geometric surface of the electrodes. Furthermore, Fig. 6b shows a cathode utilization leading to a maximum voltage value for the anode of 2.2 V *vs*. Li^+/Li (see experimental section for details). Despite the anode excess, the voltage profiles of the full-cell cycled at a current of C/3 (1C = 278 mA g^{-1} referred to the cathode mass) reported in Fig. 6c reveal a very promising behavior, with a steady-state signature reflecting the combination of anode and cathode slopes, centered at an average value of about 2.5 V with a capacity approaching 170 mAh g^{-1}. Therefore, the cell reaction pathway may be represented by the schematic equation (2):[42,47]

$$Li_yCuO + 2LiNi_{0.33}Co_{0.33}Mn_{0.33}O_2 + \rightleftharpoons Cu + xLi_2O + 2Li_{(1-x+y/2)}Ni_{0.33}Co_{0.33}Mn_{0.33}O_2 \quad (2)$$

where x is about 0.6 Li-equivalents, corresponding to a specific capacity of 170 mAh g^{-1}, and y (lower than 0.1 equivalents) is the Li content of the partially lithiated CuO (Li_yCuO), preliminarily activated up to a voltage value of 2.2 V (see experimental section and discussion of equation (1)). Fig. 6c shows a rather stable full-cell voltage profile over the 40 cycles taken into account, with only minor shift to lower voltage values of the main sloped plateau, likely due to the gradual structural changes of the anode.[11,22] This remarkable behavior is attributed to the optimized cell balance and voltage limits adopted for cell cycling (see experimental section), to the stability of the anode as well as to the suitable cathode performance in terms of voltage signature, delivered capacity and cycling stability. Fig. 6d shows the cycling trend and coulombic efficiency of the CuO/$LiNi_{0.33}Co_{0.33}Mn_{0.33}O_2$ Li-ion cell. The figure suggests partial electrolyte oxidation during the first charge with possible formation of a stable SEI layer,[42] and reveals a capacity retention as high as 97% after 40 cycles and an efficiency higher than 99%. This performance is considered remarkable, particularly taking into account the severe issues associated with the use of Li-conversion anodes in Li-ion full-cells.[11] A further investigation has been carried out by combining the CuO nano-powder anode with a $LiFePO_4$ olivine cathode which delivers a reversible capacity approaching 160 mAh g^{-1} through a flat voltage profile[58] centered at a relatively low working potential of about 3.5 V *vs*. Li^+/Li.[59] The cell has been balanced using a N/P ratio of about 1.1 in terms of capacity, corresponding to CuO and $LiFePO_4$ loadings of about 3.4 and 10.1 mg cm^{-2}, respectively, as shown in Fig. S4 of the Supporting Information, thereby allowing almost full utilization of the anode. Accordingly, the CuO/$LiFePO_4$ full-cell exhibits a wide working voltage ranging from about 0.4 to 3.4 V, which slightly decreases throughout cycling as observed for the CuO/$LiNi_{0.33}Co_{0.33}Mn_{0.33}O_2$ cell (compare Fig. S4b of the Supporting Information and Fig. 6c). The voltage curves, characterized by two steps during both charge and discharge as well as by a significant hysteresis, reflect the electrochemical features of anode and cathode (compare panels a and b of Fig. S4).

Figure 6

Therefore, we may remark that the adopted cell configuration and the N/P ratio, as well as the operating conditions in terms of voltage cutoff and C-rate, may significantly affect voltage shape, delivered capacity and stability of the full-cell.[5] Based on these considerations, further improvements may be certainly achieved by a proper cell assembling,[5] thus renewing the interest for nanometric metal oxide anodes with enhanced characteristics in terms of structure, morphology and composition.

Conclusions

Nanometric copper oxide has been thoroughly investigated for possible application as a conversion anode in Li-ion cells through a multidisciplinary approach advantageously combining electrochemical techniques and advanced X-ray tomography imaging. The nano-powder had pronounced crystallinity, with monoclinic lattice belonging to the C1c1 (9) space group, and was mostly formed by sub-micrometric agglomerates with size approaching 500 nm of nanoparticles (about 70 nm), along with relatively large, micrometric particles. Electrochemical studies showed a conversion reaction with suitable stability and remarkable charge/discharge hysteresis as typically observed for this class of anodes, in which a substantial structural change occurs during operation. Furthermore, the measurements in lithium cell revealed an increasing capacity trend by cycling, which led to a partial activation of the material. *Ex situ* X-ray nano-computed tomography suggested a substantial electrode reorganization upon cycling and gradual growth of copper oxide aggregates of lower density compared to the pristine material. In agreement with EIS, SEM and EDS investigations, three-dimensional reconstruction of the electrode throughout cycling evidenced the precipitation after 10 cycles of a thick SEI, having high Li^+ permeability reflected into remarkable cycling behavior upon 100 cycles. Indeed, the nanometric CuO ensured high capacity, with a maximum value exceeding 600 mAh g^{-1} after the activation ascribed to the beneficial effect of the electrode rearrangements. Such a performance suggested the suitability of the material for use in full-cells, which have been prepared and studied. In particular, a $CuO/LiNi_{0.33}Co_{0.33}Mn_{0.33}O_2$ lithium-ion

battery, assembled by carefully tuning the electrode masses, the N/P ratio and the voltage limits, stably delivered a capacity of about 170 mAh g^{-1} as referred to the cathode weight with an average voltage of about 2.5 V. Therefore, the cell is characterized by an energy density with respect to the cathode of about 425 Wh kg^{-1}, which may be actually reflected into a practical energy approaching the one of commercial batteries based on graphite anode and layered oxide cathode.[5] Despite a number of issues hindering the application of conversion anodes have been not fully addressed yet, our results suggested a large room for improvements of nanometric transition metal oxide anodes. Moreover, our work highlights that the suitable combination of a thorough X-ray CT study supported by SEM-EDS with electrochemical characterization via voltammetry, impedance spectroscopy and galvanostatic cycling can effectively elucidate the structural reorganization within the electrode and the evolution of the SEI upon the electrochemical process. Therefore, such an interdisciplinary method may actually provide a deep understanding of the behavior of electrode materials in lithium-ion batteries.

Experimental section

CuO nano-powder (< 50 nm by TEM, Sigma Aldrich), $LiNi_{0.33}Co_{0.33}Mn_{0.33}O_2$ (TODA), and $LiFePO_4$ (Aleees)[58] were characterized as received. X-ray diffraction (XRD) patterns of the CuO nano-powder were collected through a Bruker D8 Advance diffractometer equipped with a Cu Kα source, by performing a scan in the 2θ range between 6 and 70° at a rate of 5 s $step^{-1}$ and employing a step size of 0.02°. The CuO powder was spread on a glass sample holder for XRD. Sample morphology was investigated by using a Zeiss EVO 40 scanning electron microscope (SEM) with a LaB_6 thermionic gun and a Zeiss EM 910 transmission electron microscope (TEM) with a tungsten thermionic gun.

The electrodes were prepared by doctor-blade casting on copper (for CuO, thickness of 25 μm, MTI Corporation) or aluminum (for $LiNi_{0.33}Co_{0.33}Mn_{0.33}O_2$ and $LiFePO_4$, thickness of 15 μm, MTI Corporation) substrates of slurries formed by dispersing the active material (80 wt.%),

poly(vinylidene difluoride) binder (10 wt.%, PVDF 6020, Solef Solvay), and Super P conductive agent (10 wt.%, Timcal) in N-methyl pyrrolidone (Sigma-Aldrich). The coated foils were dried for 3 h at 70 °C on a hot plate, cut into the form of disks with diameter of 10 and 14 mm, and then dried overnight at 110 °C under vacuum. The electrode loadings were ranging from 2.5 to 3.5 mg cm^{-2} for CuO, about 4 mg cm^{-2} for $LiNi_{0.33}Co_{0.33}Mn_{0.33}O_2$, and about 10.1 mg cm^{-2} for $LiFePO_4$.

Coin-cells for galvanostatic cycling tests and three-electrode cells (T-type) for voltammetry and electrochemical impedance spectroscopy (EIS) measurements were assembled in an Ar-filled glovebox (MBraun, O_2 and H_2O content below 1 ppm), by using lithium metal disks as counter and reference electrodes, and a Whatman® GF/D glass fiber separator soaked by LP30 electrolyte solution (1M $LiPF_6$ EC:DMC 1:1 v:v). Electrodes having diameter of 14 mm (geometric area of 1.539 cm^2) and 10 mm (geometric area of 0.785 cm^2) were employed for preparing coin-cells and T-type cells, respectively. Cyclic voltammetry (CV) and EIS were performed through a VersaSTAT MC Princeton Applied Research (PAR, AMETEK) multichannel potentiostat. The CV measurement was performed on a three-electrode lithium cell with a CuO working electrode by varying the potential from 3 to 0.02 V *vs*. Li^+/Li with a scan rate of 0.1 mV s^{-1}. EIS measurements on the same cell were performed at the OCV, after the 1st, 2nd and 3rd voltammetry cycles by applying an alternate voltage signal with amplitude of 10 mV within frequency ranging from 500 kHz to 0.1 Hz. The spectra after the 1st, 2nd, and 3rd cycle were analyzed by nonlinear least squares (NLLS) method using the Boukamp package.[60] Chi-square (χ^2) values of the order of 10^{-4} and estimated errors on the resistive and pseudo-capacitive elements of the equivalent circuit lower than 10% confirm the reliability of the analysis for qualitative evaluation. Galvanostatic cycling measurements of half-cells using the CuO electrode were performed with a MACCOR Series 4000 battery test system at various C-rates (1C = 674 mA g^{-1}) within the 0.02 – 3 V voltage range. A rate capability test was carried out by galvanostatic cycling at current rates of C/10, C/5, C/3, C/2, and 1C, increasing every 5 cycles and decreasing back to C/10 after 26 cycles. The cycling behavior at constant current was evaluated at C/20, C/10, and C/5 rates.

Ex situ X-ray nano-computed tomography (CT) was performed on a pristine CuO sample as well as CuO samples after 1 and 10 galvanostatic cycles at C/5 rate (1C = 674 mA g^{-1}). The related cells were assembled by using a Celgard polyolefin separator soaked by a 1.2M $LiPF_6$, EC:EMC 1:3 v:v electrolyte solution as above reported, cycled through a MACCOR Model 4300 battery test system, and disassembled into an Ar-filled glovebox (MBraun, O_2 and H_2O content below 1 ppm). The CuO electrodes were washed with DMC (anhydrous, ≥ 99%, Sigma-Aldrich) to remove the electrolyte and dried under vacuum for 3 min. Afterwards, the electrodes were micromachined into micro-scale pillars: 1 mm disks were cut out, glued onto 1 mm stainless steel (SS) dowels using an epoxy resin (2,4,6-tris(dimethylaminomethyl)phenol, Devcon), and then milled down to pillars of about 100 μm diameter. A micromachining instrument (A Series/Compact Laser Micromachining System, Oxford Lasers) was used for both electrode cutting and milling.[61] The electrode pillars were studied by scanning electron microscopy (SEM) through a Zeiss EVO MA10 employing a tungsten thermionic gun. Further pristine CuO samples for X-ray nano-CT were prepared in order to exclude possible effects of the laser milling on the sample composition. Electrode pieces were attached on SS needles by epoxy (2,4,6-tris(dimethylaminomethyl)phenol, Devcon) and the current collector was carefully peeled off by means of a sharp razor.

Nano-CT datasets were obtained through a Zeiss Xradia 810 Ultra instrument (Carl Zeiss Inc.) equipped with a micro-focus rotating Cr anode (MicroMax-007HF, Rigaku) set at 35 kV and 25 mA. The quasi-parallel X-ray beam illuminating the sample was quasi-monochromatized at the 5.4 keV Cr Kα by a reflective capillary condenser, and a Fresnel zone plate focused the beam on a CCD detector. Nano-CT scans were performed in X-ray absorption-contrast, large-field-of-view (65×65 μm) mode with 1 voxel binning, by taking 1601 projections rotating the sample through 180° with 50 s exposure, thereby leading to a voxel size of about 63 nm. The tomographic datasets were reconstructed by the Zeiss XMReconstructor software (Carl Zeiss Inc.) employing a filtered back-projection algorithm. Non-local means and unsharp masking filters were applied to the tomograms, and sub-volumes with sizes of 600×600×800 $voxel^3$ (including the electrode surface) and

600×600×600 voxel^3 (electrode bulk) were cropped for processing. The cropped datasets were segmented into four phases, *i.e.*, pores and exterior, solid electrolyte interphase (SEI), carbon-binder domain, and copper oxide, by employing a grayscale threshold method.[38] Furthermore, two CuO domains having low and high density were identified according to the grayscale histograms. Volume renderings were computed for the datasets with sizes of 600×600×800 voxel^3, while phase volume fraction and continuous particle size distribution of the copper oxide domain were calculated as 600×600×600 voxel^3. Dataset processing, segmentation, and analysis were performed through Avizo (Visualization Sciences Group, FEI Company), while continuous particle size distribution was calculated through the ImageJ plugin XLib.[62]

The pristine CuO electrode was investigated by X-ray micro-CT through a Zeiss Xradia 520 Versa instrument (Carl Zeiss Inc.) employing a polychromatic micro-focus source and a tungsten target. The electrode was cut by means of a 1 mm diameter punch and attached on a SS dowel by epoxy resin (2,4,6-tris(dimethylaminomethyl)phenol, Devcon). The tungsten X-ray source was set at 100 kV and 85 µA and a 20X objective lens was used. Source and CCD detector distances were adjusted to obtain suitable transmission values and resolution. Micro-CT datasets were collected at binning 2, by taking 1601 projections rotating the sample through 360° with 13 s exposure, thus leading to a voxel size of 507×507×507 nm^3 and a field of view of about 470×470 µm. The tomographic datasets were reconstructed by the Scout-and-Scan™ Control System Reconstructor software (Carl Zeiss Inc.) employing a filtered back-projection algorithm.

The $LiNi_{0.33}Co_{0.33}Mn_{0.33}O_2$ electrode was studied by galvanostatic cycling in a lithium half-cell at a C/3 rate within the 2.7 – 4.4 V voltage range. In this respect, a theoretical 1C rate was calculated considering the reaction of 1 Li^+ equivalent per mol of $LiNi_{0.33}Co_{0.33}Mn_{0.33}O_2$, *i.e.*, 278 mA g^{-1}. A CuO/$LiNi_{0.33}Co_{0.33}Mn_{0.33}O_2$ lithium-ion, two-electrode, T-type cell was prepared by using a CuO anode (2.5 mg cm^{-2}) preliminary discharged and charged for 3 activation cycles at C/10 (as above described), with final charge up to a voltage value of 2.2 V, a pristine $LiNi_{0.33}Co_{0.33}Mn_{0.33}O_2$ cathode (4.0 mg cm^{-2}), and a Whatman® GF/D glass fiber separator soaked by LP30 solution (1M

$LiPF_6$ EC:DMC 1:1 v:v). The cell was cycled at a C/3 rate referred to the cathode (1C = 278 mA g^{-1}) within the 0.7 – 4.3 V voltage range. $LiFePO_4$ was tested by galvanostatic cycling in a lithium half-cell at a C/3 rate (1C = 170 mA g^{-1}) within the 2.8 – 4.0 V voltage range. A CuO/$LiFePO_4$ lithium-ion, two-electrode, T-type cell was assembled by combining a CuO anode (3.4 mg cm^{-2}) preliminary discharged and charged for 10 activation cycles at C/10 (as above described), with a final charge up to a voltage value of 2.8 V, a pristine $LiFePO_4$ cathode (10.1 mg cm^{-2}), and a Whatman® GF/D glass fiber separator soaked by LP30 solution (1M $LiPF_6$ EC:DMC 1:1 v:v). The cell was cycled at a C/3 rate referred to the cathode (1C = 170 mAh g^{-1}) within the 0.1 – 3.9 V voltage range. The Li/$LiNi_{0.33}Co_{0.33}Mn_{0.33}O_2$, Li/$LiFePO_4$, CuO/$LiNi_{0.33}Co_{0.33}Mn_{0.33}O_2$, and CuO/$LiFePO_4$ cells were tested through a MACCOR Series 4000 battery test system.

Acknowledgments

This work was founded by the grant "Fondo di Ateneo per la Ricerca Locale (FAR) 2017", University of Ferrara, and performed within the collaboration project "Accordo di Collaborazione Quadro 2015" between University of Ferrara (Department of Chemical and Pharmaceutical Sciences) and Sapienza University of Rome (Department of Chemistry). The authors acknowledge support from the EPSRC: EP/R023581/1, EP/R020973/1, EP/M009394/1 and EP/M028100/1. PRS acknowledges funds from the Royal Academy of Engineering (CIET1718/59).

References

[1] B. Scrosati, K. M. Abraham, W. Van Schalkwijk, J. Hassoun, Eds. , *Lithium Batteries*, John Wiley & Sons, Inc., Hoboken, NJ, USA, **2013**.

[2] M. Li, J. Lu, Z. Chen, K. Amine, *Adv. Mater.* **2018**, *30*, 1800561.

[3] D. Larcher, J.-M. Tarascon, *Nat. Chem.* **2014**, *7*, 19.

[4] A. Yoshino, in *Lithium-Ion Batter.* (Ed.: G. Pistoia), Elsevier, **2014**, pp. 1–20.

[5] D. Di Lecce, R. Verrelli, J. Hassoun, *Green Chem.* **2017**, *19*, 3442.

[6] N. Nitta, F. Wu, J. T. Lee, G. Yushin, *Mater. Today* **2015**, *18*, 252.

[7] P. K. Nayak, E. M. Erickson, F. Schipper, T. R. Penki, N. Munichandraiah, P. Adelhelm, H. Sclar, F. Amalraj, B. Markovsky, D. Aurbach, *Adv. Energy Mater.* **2018**, *8*, 1702397.

[8] W. Li, B. Song, A. Manthiram, *Chem. Soc. Rev.* **2017**, *46*, 3006.

[9] C. Masquelier, L. Croguennec, *Chem. Rev.* **2013**, *113*, 6552.

[10] M. D. Radin, S. Hy, M. Sina, C. Fang, H. Liu, J. Vinckeviciute, M. Zhang, M. S. Whittingham, Y. S. Meng, A. Van der Ven, *Adv. Energy Mater.* **2017**, *7*, 1602888.

[11] V. Aravindan, Y.-S. Lee, S. Madhavi, *Adv. Energy Mater.* **2015**, *5*, 1402225.

[12] B. Scrosati, J. Hassoun, Y.-K. Sun, *Energy Environ. Sci.* **2011**, *4*, 3287.

[13] I. Hasa, J. Hassoun, S. Passerini, *Nano Res.* **2017**, *10*, 3942.

[14] D. Yin, G. Huang, Z. Na, X. Wang, Q. Li, L. Wang, *ACS Energy Lett.* **2017**, *2*, 1564.

[15] H. Liu, G. Wang, J. Liu, S. Qiao, H. Ahn, *J. Mater. Chem.* **2011**, *21*, 3046.

[16] D. Larcher, C. Masquelier, D. Bonnin, Y. Chabre, V. Masson, J.-B. Leriche, J.-M. Tarascon, *J. Electrochem. Soc.* **2003**, *150*, A133.

[17] J.-M. Tarascon, P. Poizot, S. Laruelle, S. Grugeon, L. Dupont, *Nature* **2000**, *407*, 496.

[18] W. Qi, J. G. Shapter, Q. Wu, T. Yin, G. Gao, D. Cui, *J. Mater. Chem. A* **2017**, *5*, 19521.

[19] R. Khatib, A.-L. Dalverny, M. Saubanère, M. Gaberscek, M.-L. Doublet, *J. Phys. Chem. C* **2013**, *117*, 837.

[20] Q. Su, D. Xie, J. Zhang, G. Du, B. Xu, *ACS Nano* **2013**, *7*, 9115.

[21] X. Wang, D.-M. Tang, H. Li, W. Yi, T. Zhai, Y. Bando, D. Golberg, *Chem. Commun.* **2012**, *48*, 4812.

[22] J. Cabana, L. Monconduit, D. Larcher, M. R. Palacín, *Adv. Mater.* **2010**, *22*, 170.

[23] S. Wu, G. Fu, W. Lv, J. Wei, W. Chen, H. Yi, M. Gu, X. Bai, L. Zhu, C. Tan, Y. Liang, G. Zhu, J. He, X. Wang, K. H. L. Zhang, J. Xiong, W. He, *Small* **2018**, *14*, 1702667.

[24] S. H. Yu, S. H. Lee, D. J. Lee, Y. E. Sung, T. Hyeon, *Small* **2016**, *12*, 2146.

[25] G. Chen, L. Yan, H. Luo, S. Guo, *Adv. Mater.* **2016**, 7580.

[26] Q. Sun, L. Zhou, L. Sun, C. Wang, Y. Wu, X. Wang, L. Wang, J. Ming, *Chem. - A Eur. J.* **2018**, *24*, 16902.

[27] Q. Su, J. Zhang, Y. Wu, G. Du, *Nano Energy* **2014**, *9*, 264.

[28] H. Ming, H. Zhou, X. Zhu, S. Zhang, P. Zhao, M. Li, L. Wang, J. Ming, *Energy Technol.* **2018**, *6*, 766.

[29] J. Hassoun, F. Croce, I. Hong, B. Scrosati, *Electrochem. Commun.* **2011**, *13*, 228.

[30] F. Wang, R. Robert, N. A. Chernova, N. Pereira, F. Omenya, F. Badway, X. Hua, M. Ruotolo, R. Zhang, L. Wu, V. Volkov, D. Su, B. Key, M. S. Whittingham, C. P. Grey, G. G. Amatucci, Y. Zhu, J. Graetz, *J. Am. Chem. Soc.* **2011**, *133*, 18828.

[31] Q. Su, L. Yao, J. Zhang, G. Du, B. Xu, *ACS Appl. Mater. Interfaces* **2015**, *7*, 23062.

[32] M. Islam, G. Ali, M.-G. Jeong, W. Choi, K. Y. Chung, H.-G. Jung, *ACS Appl. Mater. Interfaces* **2017**, *9*, 14833.

[33] H. Xue, Z. Na, Y. Wu, X. Wang, Q. Li, F. Liang, D. Yin, L. Wang, J. Ming, *J. Mater. Chem. A* **2018**, *6*, 12466.

[34] C. Tan, T. M. M. Heenan, R. F. Ziesche, S. R. Daemi, J. Hack, M. Maier, S. Marathe, C. Rau, D. J. L. Brett, P. R. Shearing, *ACS Appl. Energy Mater.* **2018**, *1*, 5090.

[35] O. O. Taiwo, J. M. Paz-García, S. A. Hall, T. M. M. Heenan, D. P. Finegan, R. Mokso, P. Villanueva-Pérez, A. Patera, D. J. L. Brett, P. R. Shearing, *J. Power Sources* **2017**, *342*, 904.

[36] C. Tan, M. D. R. Kok, S. R. Daemi, D. J. L. Brett, P. R. Shearing, *Phys. Chem. Chem. Phys.* **2019**, *21*, 4145.

[37] O. O. Taiwo, M. Loveridge, S. D. Beattie, D. P. Finegan, R. Bhagat, D. J. L. Brett, P. R. Shearing, *Electrochim. Acta* **2017**, *253*, 85.

[38] T. M. M. Heenan, J. J. Bailey, X. Lu, J. B. Robinson, F. Iacoviello, D. P. Finegan, D. J. L. Brett, P. R. Shearing, *Fuel Cells* **2017**, *17*, 75.

[39] H. Bin Wu, J. S. Chen, H. H. Hng, X. Wen (David) Lou, *Nanoscale* **2012**, *4*, 2526.

[40] F. Jiao, J. Bao, P. G. Bruce, *Electrochem. Solid-State Lett.* **2007**, *10*, A264.

[41] R. Verrelli, J. Hassoun, *J. Power Sources* **2015**, *299*, 611.

[42] D. Di Lecce, P. Andreotti, M. Boni, G. Gasparro, G. Rizzati, J.-Y. Hwang, Y.-K. Sun, J. Hassoun, *ACS Sustain. Chem. Eng.* **2018**, *6*, 3225.

[43] J. Hassoun, F. Bonaccorso, M. Agostini, M. Angelucci, M. G. Betti, R. Cingolani, M. Gemmi, C. Mariani, S. Panero, V. Pellegrini, B. Scrosati, *Nano Lett* **2014**, *14*, 4901.

[44] A. Débart, L. Dupont, P. Poizot, J.-B. Leriche, J. M. Tarascon, *J. Electrochem. Soc.* **2001**, *148*, A1266.

[45] R. Sahay, P. Suresh Kumar, V. Aravindan, J. Sundaramurthy, W. Chui Ling, S. G. Mhaisalkar, S. Ramakrishna, S. Madhavi, *J. Phys. Chem. C* **2012**, *116*, 18087.

[46] R. Verrelli, J. Hassoun, A. Farkas, T. Jacob, B. Scrosati, *J. Mater. Chem. A* **2013**, *1*, 15329.

[47] D. Di Lecce, R. Verrelli, D. Campanella, V. Marangon, J. Hassoun, *ChemSusChem* **2017**, *10*, 1607.

[48] L. Martin, H. Martinez, D. Poinot, B. Pecquenard, F. Le Cras, *J. Phys. Chem. C* **2013**, *117*, 4421.

[49] N. Pereira, L. Dupont, J. M. Tarascon, L. C. Klein, G. G. Amatucci, *J. Electrochem. Soc.* **2003**, *150*, A1273.

[50] A. Ponrouch, P.-L. Taberna, P. Simon, M. R. Palacín, *Electrochim. Acta* **2012**, *61*, 13.

[51] A. Ponrouch, J. Cabana, R. Dugas, J. L. Slack, M. R. Palacín, *RSC Adv.* **2014**, *4*, 35988.

[52] D. Di Lecce, R. Verrelli, J. Hassoun, *Electrochim. Acta* **2016**, *220*, 384.

[53] K. E. Gregorczyk, Y. Liu, J. P. Sullivan, G. W. Rubloff, *ACS Nano* **2013**, *7*, 6354.

[54] Y. Ma, U. Ulissi, D. Bresser, Y. Ma, Y. Ji, S. Passerini, *Electrochim. Acta* **2017**, *258*, 535.

[55] H. Fu, Z. Xu, T. Wang, K. Li, X. Shen, J. Li, J. Huang, *J. Electrochem. Soc.* **2018**, *165*, A439.

[56] M. Gauthier, T. J. Carney, A. Grimaud, L. Giordano, N. Pour, H.-H. Chang, D. P. Fenning, S. F. Lux, O. Paschos, C. Bauer, F. Maglia, S. Lupart, P. Lamp, Y. Shao-Horn, *J. Phys. Chem. Lett.* **2015**, *6*, 4653.

[57] L. Martin, H. Martinez, D. Poinot, B. Pecquenard, F. Le Cras, *J. Power Sources* **2014**, *248*,

861.

[58] S. Brutti, J. Hassoun, B. Scrosati, C.-Y. Y. Lin, H. Wu, H.-W. W. Hsieh, *J. Power Sources* **2012**, *217*, 72.

[59] D. Di Lecce, J. Hassoun, *J. Phys. Chem. C* **2015**, *119*, 20855.

[60] B. A. Boukamp, *Solid State Ionics* **1986**, *20*, 31.

[61] J. J. Bailey, T. M. M. Heenan, D. P. Finegan, X. Lu, S. R. Daemi, F. Iacoviello, N. R. Backeberg, O. O. Taiwo, D. J. L. Brett, A. Atkinson, P. R. Shearing, *J. Microsc.* **2017**, *267*, 384.

[62] B. Münch, L. Holzer, *J. Am. Ceram. Soc.* **2008**, *91*, 4059.

Figure captions

Figure 1. (**a**) X-ray diffraction (XRD) patterns and photographic image (inset) of the nanometric CuO powder. (**b**-**c**) Scanning electron microscopy (SEM) and (**c**-**d**) transmission electron microscopy (TEM) images of the nanometric CuO powder. Inset of panel **e**: selected area diffraction pattern (SADP) of the nanometric CuO particles.

Figure 2. (**a**) Cyclic voltammetry and (**b**) electrochemical impedance spectroscopy (EIS) Nyquist plots with magnification at medium-high frequency of a three-electrode lithium cell using CuO as the working electrode. Cyclic voltammetry performed within 0.02 – 3.0 V *vs*. Li^+/Li using a scan rate of 0.1 mV s^{-1}. EIS performed at the OCV, after the first, second and third voltammetry cycle by applying an alternate voltage signal with amplitude of 10 mV in frequency range from 500 kHz to 0.1 Hz.

Figure 3. Cycling performance of the CuO electrode in lithium cells using LP30 (EC:DMC 1:1 v:v, $LiPF_6$) as the electrolyte within the 0.02 – 3 V range. (**a**, **b**) Rate capability test at C-rates of C/10, C/5, C/3, C/2 and 1C (C = 674 mA g^{-1}) in terms of (**a**) voltage profiles at the steady state and (**b**) cycling behavior. Inset of panel **a** reports the voltage profile of the first cycle at C/10. (**c**, **e**, **g**) Galvanostatic voltage profiles and (**d**, **f**, **h**) corresponding cyclic behavior of tests performed at (**c-d**) C/20, (**e-f**) C/10, and (**g-h**) C/5 rate (1C = 674 mA g^{-1}). (**b**, **d**, **f**, **h**) Cell capacity on the left and coulombic efficiency on the right y-axes.

Figure 4. *Ex situ* X-ray nano-CT study of CuO electrode. (**a-c**) Cross-sectional slices extracted in a plane orthogonal to the current collector for (**a**) pristine CuO, (**b**) CuO after 1 cycle, and (**c**) CuO after 10 cycles. (**d**) Grayscale histogram for the datasets. (**e-g**) Four-phase segmentation of the slices in panels **a-c** for (**e**) pristine CuO, (**f**) CuO after 1 cycle, and (**g**) CuO after 10 cycles (black: pores; grey: carbon-binder; light red: low density CuO; dark red: high-density CuO). Voxel size: 63^3 nm^3; Dataset size: 600×600×800 $voxel^3$. (**h**) Phase volume fractions of cropped datasets (600×600×600 $voxel^3$). Microfocus rotating anode X-ray source set at 35 kV and 25 mA. Scans performed in X-ray

absorption-contrast and large-field-of view (65 μm) modes, by taking 1601 projections through 180° with 50 s exposure and 1 voxel binning.

Figure 5. *Ex situ* X-ray nano-CT study of CuO electrode. (**a**-**c**) Volume rendering for (**a**) pristine CuO, (**b**) CuO after 1 cycle, and (**c**) CuO after 10 cycles. Voxel size: 63^3 nm^3; Dataset size: 600×600×800 nm^3. (**d**,**e**) Continuous particle size distribution of (**d**) high-density and (**e**) low-density CuO for a cropped datasets (600×600×600 $voxel^3$). Microfocus rotating anode X-ray source set at 35 kV and 25 mA. Scans performed in X-ray absorption-contrast and large-field-of view (65 μm) modes, by taking 1601 projections through 180° with 50 s exposure and 1 voxel binning.

Figure 6. (**a**) Cycling trend and voltage profile (inset) of the $LiNi_{0.33}Co_{0.33}Mn_{0.33}O_2$ electrode in lithium half-cell galvanostatically cycled at a C-rate of C/3. (**b**) Galvanostatic voltage profiles of a steady-state cycle of lithium half-cells using $LiNi_{0.33}Co_{0.33}Mn_{0.33}O_2$ (red curve) and CuO (blue curve) cycled at C/3 and C/10 rates, respectively, used for determining the cell balance. Bottom x-axis reports the areal capacity of the cell (mAh cm^{-2}) as referred to the electrode geometric area (1.54 cm^{-2}), while top x-axis reports the specific capacity of the cell (mAh g^{-1}) as referred to the cathode weight. The half-cells mass loadings are reported in inset. (**c**) Voltage profile and (**d**) cycling behavior of the CuO/$LiNi_{0.33}Co_{0.33}Mn_{0.33}O_2$ full-cell cycled at a C-rate of C/3. Both C-rate and capacity of the full-cell are referred to the cathode weight. The values of 1C current are 278 mA g^{-1} for the $LiNi_{0.33}Co_{0.33}Mn_{0.33}O_2$ half-cell and for the CuO/$LiNi_{0.33}Co_{0.33}Mn_{0.33}O_2$ full-cell, and 674 mA g^{-1} for CuO half-cell, while the voltage limits are 0.02 – 3.0 V for CuO half-cell, 2.7 – 4.4 V for $LiNi_{0.33}Co_{0.33}Mn_{0.33}O_2$ half-cell and 0.7 – 4.3 V for the CuO/$LiNi_{0.33}Co_{0.33}Mn_{0.33}O_2$ full-cell.

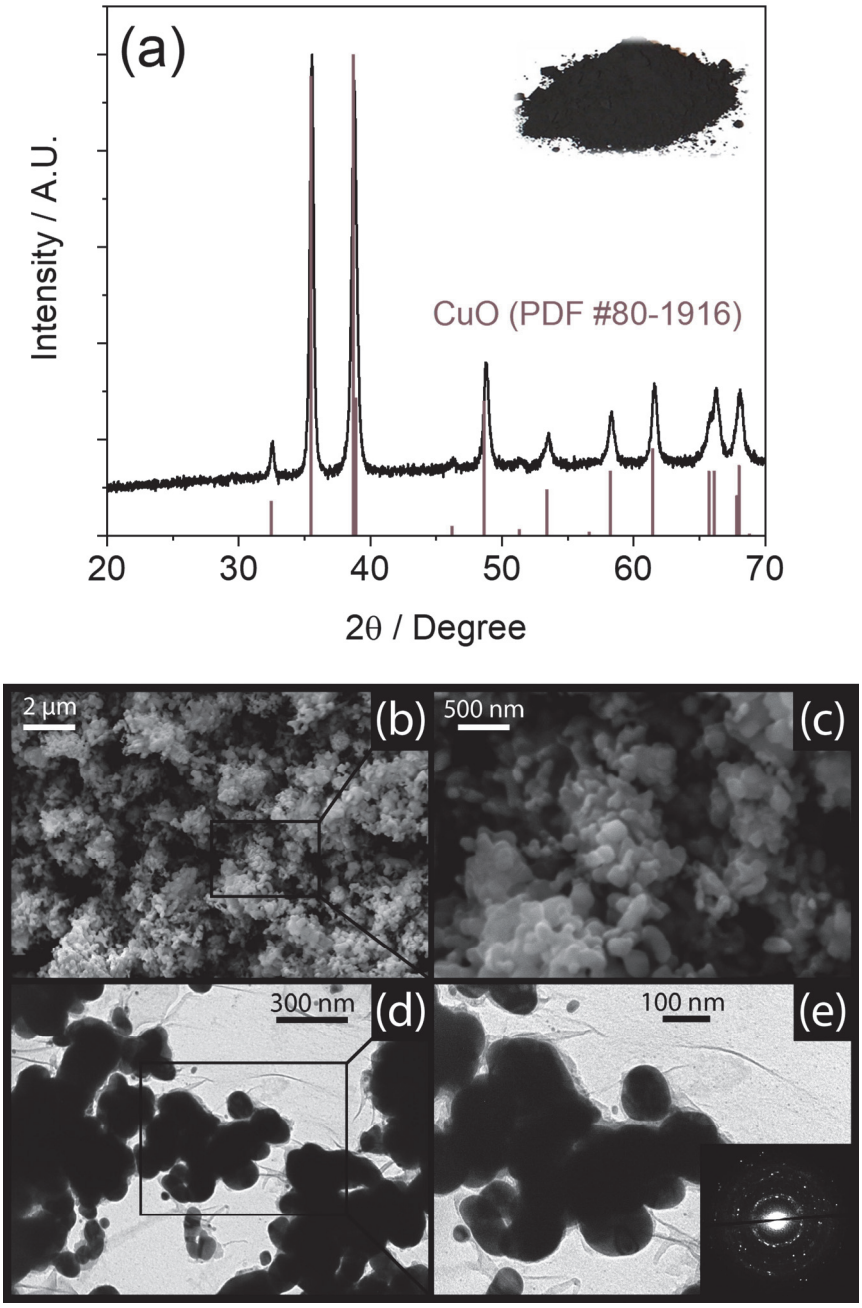
(a)
Intensity / A.U.
CuO (PDF #80-1916)
20
30
40
50
60
70
2θ / Degree
2 μm
(b)
500 nm
(c)
300 nm
(d)
100 nm
(e)

Figure 1

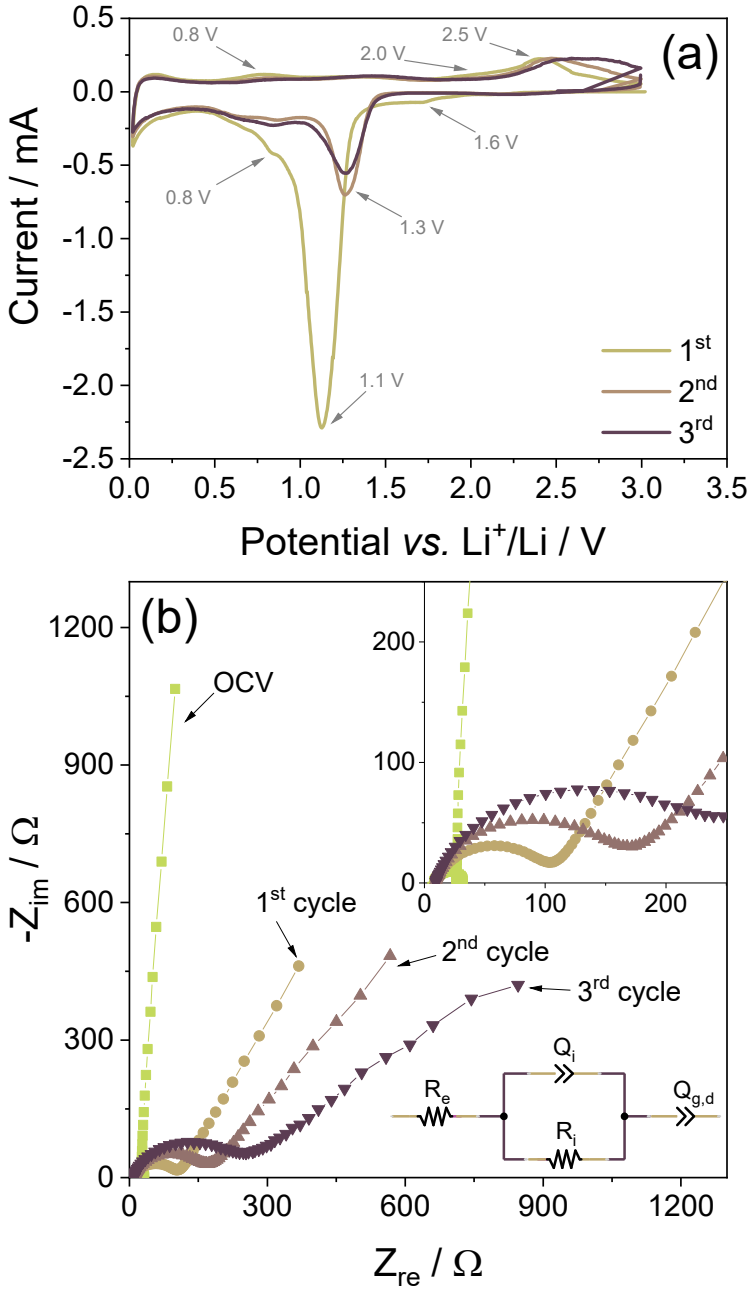
(a)
0.8 V
2.0 V
2.5 V
1.6 V
0.8 V
1.3 V
1.1 V
1st
2nd
3rd
Current / mA
Potential vs. Li+/Li / V
(b)
OCV
1st cycle
2nd cycle
3rd cycle
Qi
Re
Ri
Qg,d
-Zim / Ω
Zre / Ω

Figure 2

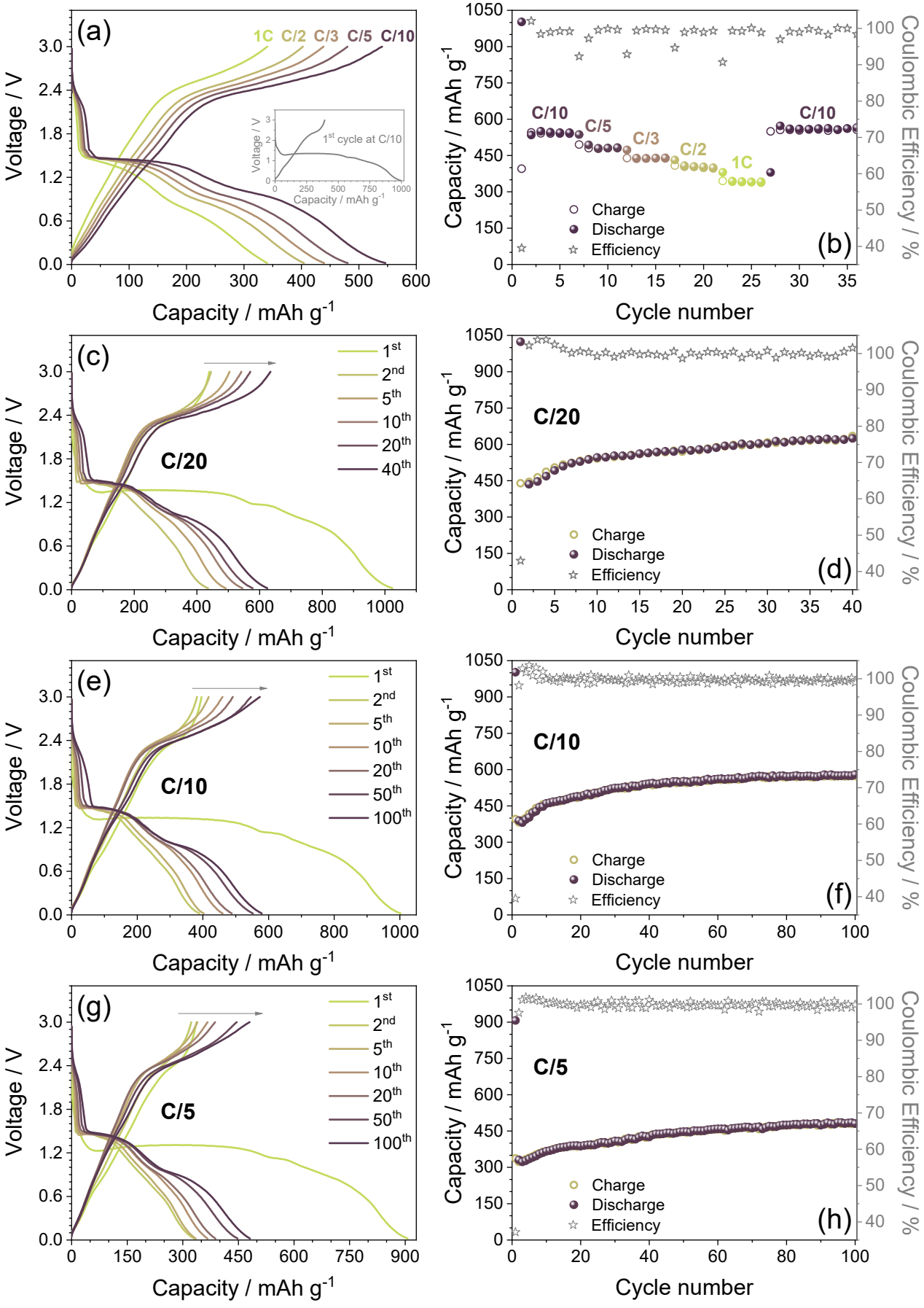
(a)
1C C/2 C/3 C/5 C/10
Voltage / V
Capacity / mAh g-1
1st cycle at C/10
(b)
C/10 C/5 C/3 C/2 1C C/10
Charge
Discharge
Efficiency
Capacity / mAh g-1
Coulombic Efficiency / %
Cycle number
(c)
C/20
1st 2nd 5th 10th 20th 40th
(d)
(e)
C/10
1st 2nd 5th 10th 20th 50th 100th
(f)
(g)
C/5
(h)

Figure 3

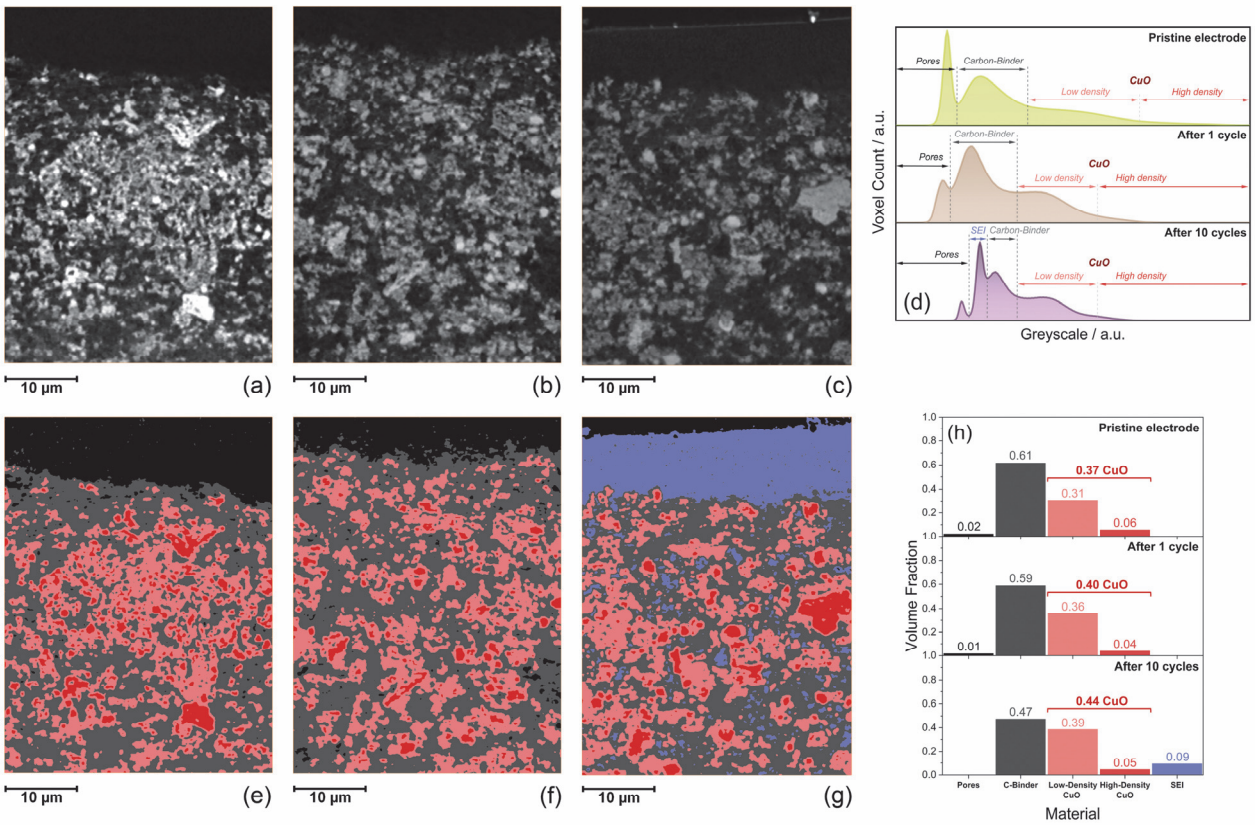
10 µm
(a)
10 µm
(b)
10 µm
(c)
Pristine electrode
Pores
Carbon-Binder
CuO
Low density
High density
After 1 cycle
Carbon-Binder
Pores
CuO
Low density
High density
After 10 cycles
SEI Carbon-Binder
Pores
CuO
Low density
High density
(d)
Voxel Count / a.u.
Greyscale / a.u.
10 µm
(e)
10 µm
(f)
10 µm
(g)
(h)
Pristine electrode
0.61
0.37 CuO
0.31
0.06
0.02
After 1 cycle
0.59
0.40 CuO
0.36
0.04
0.01
After 10 cycles
0.47
0.44 CuO
0.39
0.05
0.09
Volume Fraction
Pores
C-Binder
Low-Density CuO
High-Density CuO
SEI
Material

Figure 4

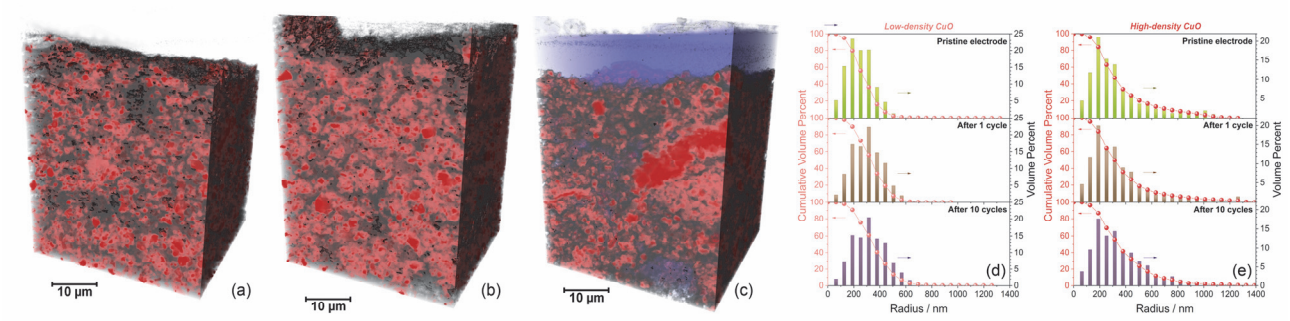
10 μm
(a)
10 μm
(b)
10 μm
(c)
Low-density CuO
High-density CuO
Pristine electrode
After 1 cycle
After 10 cycles
Cumulative Volume Percent
Volume Percent
Radius / nm
(d)
(e)

Figure 5

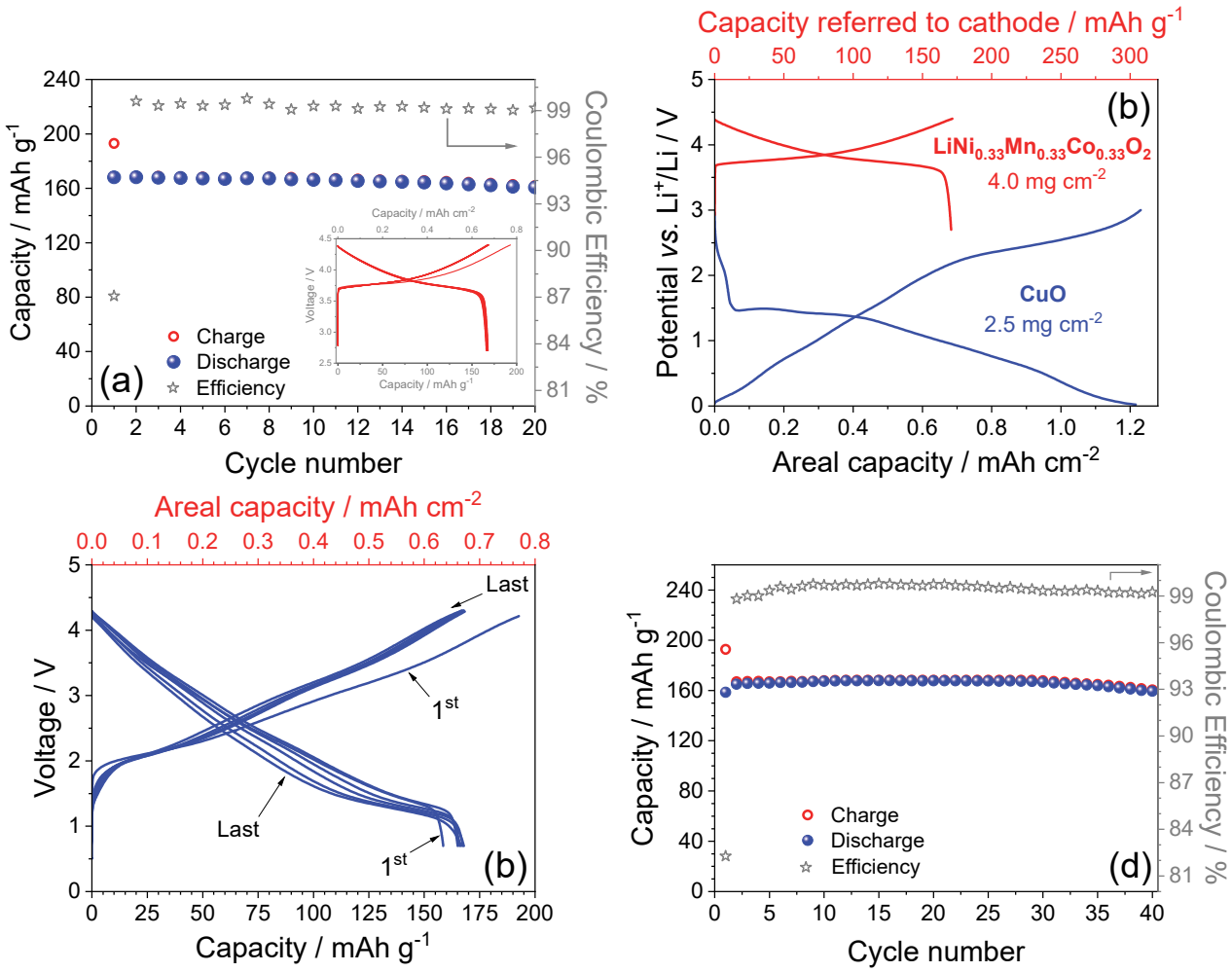
Capacity / mAh g-1
Coulombic Efficiency / %
Cycle number
Charge
Discharge
Efficiency
(a)
Capacity / mAh cm-2
Voltage / V
Capacity / mAh g-1
Capacity referred to cathode / mAh g-1
Potential vs. Li+/Li / V
LiNi0.33Mn0.33Co0.33O2
4.0 mg cm-2
CuO
2.5 mg cm-2
(b)
Areal capacity / mAh cm-2
Last
1st
(b)
(d)

Figure 6